

Lattice-Boltzmann simulation of coaxial jet noise generation

By D. Casalino[†] AND S. K. Lele

A Lattice-Boltzmann model for high-speed non-isothermal subsonic flows is used to simulate the unsteady jet exhausting from a short-cowl axisymmetric coaxial nozzle and the associated noise. The primary and secondary jet exit Mach numbers are 0.87 and 0.90, respectively, the secondary jet Reynolds number is $2.8 \cdot 10^6$, and the primary to secondary temperature ratio is 2.7. The far-field is computed through a Ffowcs-Williams and Hawkings analogy applied to a fluid surface encompassing the plume. Numerical results are presented for one exhaust condition and for one grid resolution only; in this respect, the main achievements of the present effort are a sanity check of the simulation setup and a first stage of a grid resolution study. The presented near- and far-field results confirm that the underlying flow features are reasonably represented by the numerical solution. Areas of required improvements have been clearly identified in the growth rate of the shear-layer turbulent fluctuations and will be the main objective of future studies. More in general, the sensitivity of the jet turbulent properties to the mesh resolution will be investigated and published in the future as a completing part of the present work.

1. Introduction

Despite the greater industrial relevance of double-stream nozzle flows compared to single-stream flows, less research effort has focused on the analysis of the noise generation mechanisms taking place within coaxial nozzle jets. From a flow physics point of view, the dual-stream jets are affected by the strong interaction between two turbulent shear layers, thus resulting in a different distribution of the turbulent kinetic energy in the plume compared to a single-stream jet. Moreover, the primary stream of coaxial jets is usually strongly heated, which might affect the noise sources according to the controversial debate about the existence of entropy dipolar sources (Viswanathan 2004). In a dual-stream jet, in fact, the interaction and amalgamation process between cold and hot turbulent eddies leads to a different thermal mixing than in a single-stream jet where the ambient cold air is passively entrained by the hot shear-layer eddies. Therefore, the space-time spectral properties of the entropy fluctuations can be different in single and coaxial jet flows.

Recently, Tinney & Jordan (2008) analyzed measurements performed in the near pressure fields of a coaxial short-cowl nozzle, with and without serration on the secondary nozzle lip, and for three exit conditions. By separating the convective and acoustic spectral components, they observed two distinct signatures in the acoustic component of the field: a low-frequency component that primarily radiates at small angles to the flow axis and is characterized by a large axial coherence, and a high-frequency component that primarily radiates in sideline directions and has a less coherent behavior. Another outcome of that study was that increasing the velocity and temperature of the primary jet results in higher acoustic components and almost unchanged hydrodynamic components. Therefore, the authors argued that the hydrodynamic near field is mainly driven by the

[†] Aerospace, Exa Corporation, Germany

turbulent eddies in the secondary shear layer, whereas the acoustic field is mostly generated by the interaction between the two shear layers. This argument is supported by the hypothesis that the local Mach number of the core jet is subsonic with respect to the core temperature, while its velocity is supersonic with respect to the ambient conditions, making its instability wave components a potentially more important source of sound.

The measurements used in (Tinney & Jordan 2008) were performed in the QinetiQ Noise Test Facility in the framework of the research program CoJeN funded by the European Commission. Together with other small-scale coaxial jet noise measurements acquired at the University of Poitiers (Guitton *et al.* 2007), the CoJeN project provided a big impulse to the validation of several CFD methods for the prediction of coaxial jets based on large-eddy simulations (Fayard *et al.* 2008; Bogey *et al.* 2009; Koh *et al.* 2009) and detached-eddy simulations (Eschricht *et al.* 2008). Previous large-eddy simulations of coaxial jets have been carried out by Andersson *et al.* (2005), Vuillemin *et al.* (2005), Viswanathan *et al.* (2006), Mihaescu *et al.* (2006), and Tristante *et al.* (2006).

Similarly to Fayard *et al.* (2008), the present work makes use of the QinetiQ measurements reported by Tinney & Jordan (2008). Simulations are performed by using a high-speed non-isothermal Lattice Boltzmann Method (LBM) implemented in a beta release version of the software PowerFLOW 5.1 developed by Exa Corporation. The same version of the solver has been used recently by Lew *et al.* (2014) and by Casalino *et al.* (2014c) to compute the noise generated by single jets and by Habibi *et al.* (2014) for a more complex dual-stream nozzle configuration consisting in a buried primary nozzle with a lobed lip. The goal of the present work is therefore to complete the jet-noise validation portfolio of the LB solver before integration of fan and jet noise sources into a comprehensive turbofan aeroacoustic simulation, as in (Casalino *et al.* 2014c).

This paper is organized as follows. The LB flow model is briefly outlined in Section 2. Section 3 describes the coaxial jet configuration and the simulation setup. Time-averaged and unsteady near-field results are presented in Section 4; only a subset of results are presented, those for which published experimental data are available. Acoustic results are shown in Section 5. Finally, the main outcomes of the present study and possible directions for improvement are summarized in Section 6.

2. Lattice-Boltzmann flow model

The physical core of PowerFLOW solves the Boltzmann equation for the distribution function $f(\mathbf{x}, t, \mathbf{v})$ on a hexahedral mesh automatically generated around bodies consisting of one or more connected solid parts. The function f represents the probability of finding, in the elementary volume $d\mathbf{x}$ around \mathbf{x} and in the infinitesimal time interval $(t, t + dt)$, a number of fluid particles with velocity in the interval $(\mathbf{v}, \mathbf{v} + d\mathbf{v})$. The Boltzmann equation is solved by discretizing the particle velocity space into a prescribed number of values \mathbf{v}_i , in magnitude and direction. These discrete velocity vectors are such that, in a prescribed time step Δt , one particle is advected from one point of the mesh to 19 neighboring points, including the point itself, which constitute the computational stencil of the so-called D3Q19 scheme (three-dimensional 19 states model). The standard LBM formulation is based on the time-explicit advection equation $f_i(\mathbf{x} + \mathbf{v}_i \Delta t, t + \Delta t) - f_i(\mathbf{x}, t) = C_i(\mathbf{x}, t)$, where f_i is the probability for particles to travel at speed v_i from the position \mathbf{x} at time t in the discrete direction i . The collision term C is modeled with the well-known Bhatnagar-Gross-Krook (BGK) approximation (Bhatnagar *et al.* 1954; Chen *et al.* 1992). i.e $C_i(\mathbf{x}, t) = [f_i(\mathbf{x}, t) - f_i^{\text{eq}}(\mathbf{x}, t)] / \tau$, where τ is the relaxation time, which is related to the fluid viscosity, and f_i^{eq} is the equilibrium distribution, which is approximated by a third-order expansion with constant temperature

(Chen & Teixeira 2000). Once the distribution function is computed, flow density and linear momentum, are simply determined through discrete integration $\rho(\mathbf{x}, t) = \sum_i f_i(\mathbf{x}, t)$ and $\rho\mathbf{u}(\mathbf{x}, t) = \sum_i f_i(\mathbf{x}, t) \mathbf{v}_i$. All the other quantities are determined through thermodynamic relationships for an ideal gas. It can be demonstrated that using 19 particle velocity states ensures sufficient lattice symmetry to recover the Navier-Stokes equations for an isentropic (isothermal) flow (Chen *et al.* 1992). The isothermal assumption reduces the limit of validity of the D3Q19 scheme to a free-stream Mach number value of about 0.4. In order to extend the dynamic range of the D3Q19 scheme, the isothermal assumption is removed by introducing a regularized collision operator and solving an additional energy equation as described in (Nie *et al.* 2009).

Solving the lattice Boltzmann equation is equivalent to performing a direct numerical simulation of the Navier-Stokes equations in the limits of the dynamic range (Mach number) that can be accurately covered by the number of discrete particle velocity vectors, and in the limits of the lattice resolution required to capture the smallest scales of turbulence. For high Reynolds flows, turbulence modeling is introduced (Chen *et al.* 2003) by solving a variant of the RNG $k - \epsilon$ model (Yakhot & Orszag 1986; Yakhot *et al.* 1992) on the unresolved scales (Teixeira 1998), selected via a swirl model (Alexander *et al.* 2001), a method referred to as LBM Very Large Eddy Simulation (LBM-VLES).

The LBM scheme is solved on a grid composed of cubic volumetric elements (voxels). A variable resolution by a factor of two is allowed between adjacent regions. Consistently, the time step is varied by a factor two between adjacent resolution regions. Solid surfaces are automatically facetized within each voxel intersecting the wall geometry using planar surface elements (surfels). For the no-slip and slip wall boundary conditions at each of these elements, a boundary scheme (Chen *et al.* 1998) is implemented, based on a particle bounce-back process and a specular reflection process, respectively. Thereby, very complex arbitrary geometries can be treated automatically by the LBM solver.

The local character of the LBM scheme allows an efficient parallelization of the solver. Moreover, thanks to the intrinsically low dissipative properties of the scheme (Marié *et al.* 2009), LBM is particularly suited for aeroacoustic simulations and, especially, for airframe noise applications (Casalino *et al.* 2014*a,b*; Khorrami *et al.* 2014).

Although the LBM has intrinsic CAA capabilities and can compute the noise propagation directly from the unsteady flow simulations, this approach is generally computationally expensive and limited to the near field. Therefore, in order to compute the far-field noise, an integral extrapolation based on the Ffowcs-Williams and Hawkings (FW-H) acoustic analogy is used (Brès *et al.* 2010), solved in forward time (Casalino 2003).

3. Nozzle geometry, flow conditions, and numerical setup

The coaxial nozzle geometry is the same as that described in (Tinney & Jordan 2008). The primary and secondary nozzle diameters are $D_p=135.9$ mm and $D_s=273.4$ mm, respectively, and the corresponding lips have a thickness of 0.92 mm and 1.20 mm. Figure 1 shows the computational domain and the Variable Resolution (VR) mesh boundaries in the vicinity of the nozzle, from the coarsest (VR8) to the finest plotted (VR10), which covers the plume entirely. Finer VR levels from 11 to 14 are generated by offsetting the internal surfaces of the nozzle in the wall-normal direction, thus resulting in the mesh layout of Figure 2. Overall, 15 VR levels are used, the mesh resolution varying by a factor of two from two adjacent VR levels. One mesh resolution is considered in this study, corresponding to a cell size of $D_s/64$ in the plume. The computational domain extends over about $850 D_s$ along the x direction, and $700 D_s$ along the y and z directions. Numerical sponge buffers are used in the outer part of the simulation domain to enforce

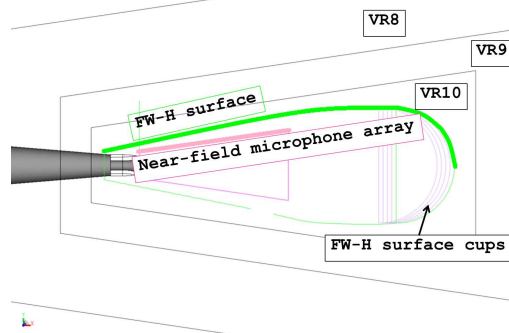


FIGURE 1. Mesh layout and near-field data sampling regions.

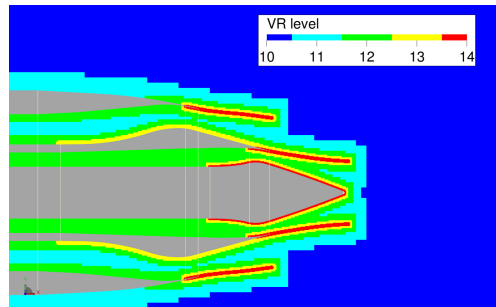


FIGURE 2. Mesh layout close to the nozzle with colors denoting different VR regions.

an anechoic behavior. As depicted in Figure 1, two axisymmetric data sampling surfaces are included in this region: the FW-H integration surface and the near-field microphone surface. The second one is obtained by revolution of a straight line that reproduces the linear microphone array used in the experiments. The voxel size and the corresponding time step in the plume are such that data sampled on these surfaces guarantee a frequency cutoff of about 8 kHz. The downstream termination of the FW-H surface is equipped with five staggered cups that, by averaging the far-field noise signals, would allow filtering the signature of the vortical perturbations passing through the integration surface, as proposed by Shur *et al.* (2005) and more recently by Mendez *et al.* (2013).

After mesh generation by intersection between the imported surface mesh and the Cartesian mesh, the number of generated voxels and surfels are $431 \cdot 10^6$ and $19 \cdot 10^6$, respectively. A physical time of 0.243 s is simulated, and the overall amount of CPU hours is $50 \cdot 10^3$, corresponding to a wall clock time of about three days on 720 cores. The simulation is seeded from a previous simulation on a coarser mesh, and a settling transient of 0.0185 s is discarded from the data analysis process.

The free-stream and nozzle exhaust conditions are listed in Table 1. The fluid viscosity is evaluated using the Sutherland's law. The superscript 0 denotes stagnation quantities. The Reynolds numbers Re are based on the corresponding nozzle diameters. M_a and T_r denote the acoustic Mach number (U/c_∞) and the static temperature ratio (T/T_∞). The free-stream conditions are $T_\infty=291.3$ K and $p_\infty=101325$ Pa.

The employed exit conditions match the nominal experimental conditions and might differ from the actual exit conditions during the measurements. This difference, together with the fact that no information is available about the exhaust boundary layer prop-

	p^0	T^0	M	M_a	T_r	Re	\bar{M}	\tilde{M}	\bar{T}	\tilde{T}
free-stream (∞)	101332.1	291.3	0.010	0.010	1	-	-	-	-	-
primary jet (p)	165526.7	880.0	0.868	1.406	0.989	$8.5 \cdot 10^5$	0.65%	0.23%	2.18%	0.06%
secondary jet (s)	171788.3	335.0	0.902	0.897	2.626	$2.8 \cdot 10^6$	4.35%	0.05%	1.38%	0.01%

TABLE 1. Free-stream and jet exhaust conditions and percentage variations of exhaust Mach number and temperature from the nominal exit conditions. Overline and tilde denote time-averaged and standard deviation, respectively. All quantities in SI units.

erties, can be a significant source of uncertainties. The nominal exit values are used to compute the total pressure and temperature imposed at the nozzle inlets by solving quasi-one-dimensional gas dynamics and incorporating very small drops in total pressure and total temperature into the formulas to account for the viscous losses along the ducts. These losses are calibrated only once during the initial stage of the simulation. No attempt has been made to dynamically track the nominal exit conditions. As a consequence, small deviations from the nominal prescribed conditions have been registered; time-averaged and standard deviation values of the percentage variation of Mach number and temperature at the midpoint of the primary and secondary exhausts are reported in Table 1.

Note that the reported numerical results have been obtained without any numerical forcing of the jet and that the transition to a turbulent regime takes place spontaneously in both the primary and secondary shear layers.

4. Near-field results

This section focuses on the near-field results. Throughout, the origin of the x axis is located at the secondary lip plane. Time-averaged axial velocity extracted along transversal cuts is compared to LDV measurements in Figure 3. The first two line cuts closest to the nozzle exhibit a small overestimation of the primary core velocity, in agreement with the positive deviation of the exhaust Mach number reported in Table 1. The velocity profiles in the central part of the plume exhibit an underestimation of the peak values that can be explained by a premature mixing of the core jet with the slower secondary jet. Finally, the recovery velocity profile in the fully developed part is in very good agreement with the measurements. Profiles of the fluctuation velocity computed as $u' = \sqrt{0.5(\tilde{u}^2 + \tilde{v}^2) + 2K/3}$, with \tilde{u} and \tilde{v} denoting standard deviation of in-plane velocity components and K the modeled (unresolved) turbulent kinetic energy, are also plotted in Figure 3 and compared to LDV measurements. The contribution of the unresolved turbulence scales to the overall kinetic energy is small but not negligible. Along the centerline, for instance, the maximum values of $0.5(\tilde{u}^2 + \tilde{v}^2)$ and $2K/3$ are $2237 \text{ m}^2/\text{s}^2$ and $175 \text{ m}^2/\text{s}^2$, respectively. Two main deficiencies in the numerical prediction can be pointed out: (i) an overestimation of the fluctuation levels in the secondary shear layer close to the nozzle, revealing a faster growth of the turbulence levels; (ii) underestimated levels close to the centerline in the developed part of the plume, which are mostly due to a premature achievement of the maximum fluctuation levels. The same quantities extracted along the jet centerline and plotted in Figure 4 confirm previous observations, in particular, the location of maximum turbulent kinetic energy, and thus the length of the jet core, is underestimated by a factor of 30%, whereas the maximum velocity fluctuation level is underestimated by 24%. The large underestimation of the centerline fluctuation

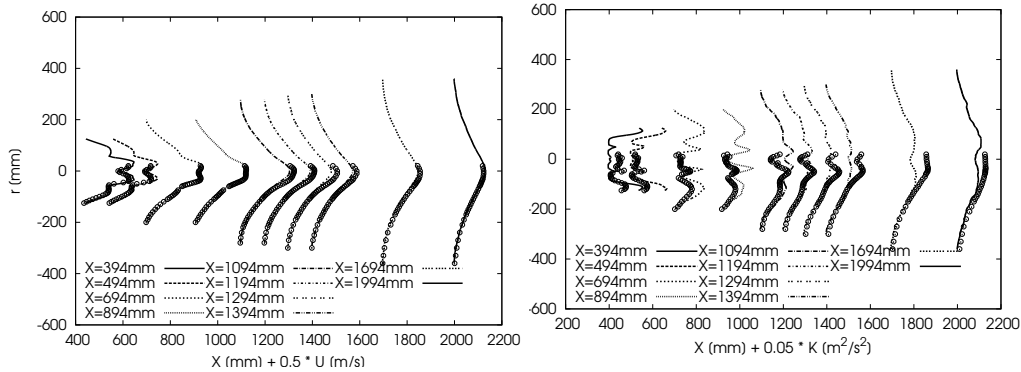


FIGURE 3. Time-averaged axial velocity (left) and turbulent kinetic energy (right) along transversal line cuts. Comparison between measurement (symbols) and LBM prediction (lines).

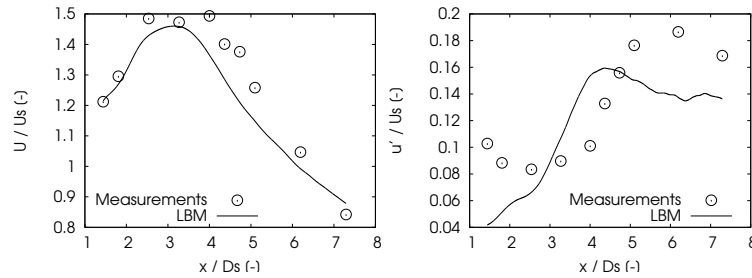


FIGURE 4. Axial velocity (left) and fluctuating velocity (right) along the jet centerline.

levels in the developed part of the plume (Figure 3) is due to the combined effect of premature mixing and lower fluctuation levels.

Contour plots of the time-averaged acoustic Mach number, temperature ratio, and velocity fluctuation are shown in Figure 5. Since the centerbody generates a wake, the accuracy of the flow solution along the centerline is expected to be affected by the proper simulation of the boundary layer development along the centerbody. Finally, the Overall Sound Pressure Level (OASPL) computed from the pressure fluctuations sampled along the near-field microphone surface and extracted along four lines staggered by 90° are compared with measurements in Figure 6. By stretching the prediction curve by 1.4 to compensate for the 70% underestimation of the low-fluctuation core length, we can obtain a better agreement with the measurement (figure on the right). The location of the maximum pressure fluctuation along the near-field array is in fact directly determined by the location of the maximum turbulent fluctuation levels in the plume. Three main different errors can be pointed out. The first is an underestimation of about 2 dB of the main radiation lobe that can be explained by the underestimated turbulence levels in the plume. The second error is the presence of a secondary radiation lobe in the numerical results with maximum at about $2D_s$, which is due to the onset of strong coherent structures in the initial part of the secondary shear layer. Finally, the third error is an underestimation of about 4 dB of the silent cone level from 0 to $1D_s$ and this could be due to the absence of additional noise-generation mechanisms in the numerical solution, such as the trailing edge noise induced by boundary layer fluctuations convected past the secondary lip. More in general, we can argue that higher background turbulence levels are present in both the primary and secondary exhausts, as also revealed by the under-

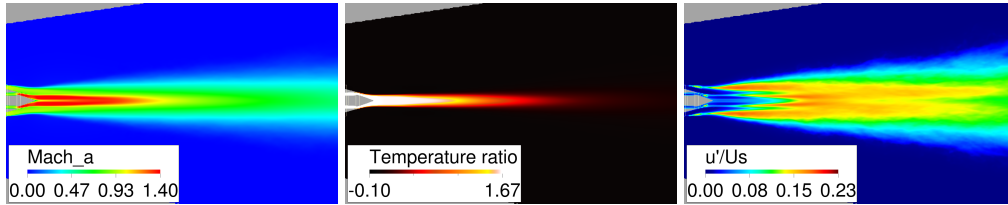


FIGURE 5. Acoustic Mach number (left), temperature (middle) and velocity fluctuation (right).

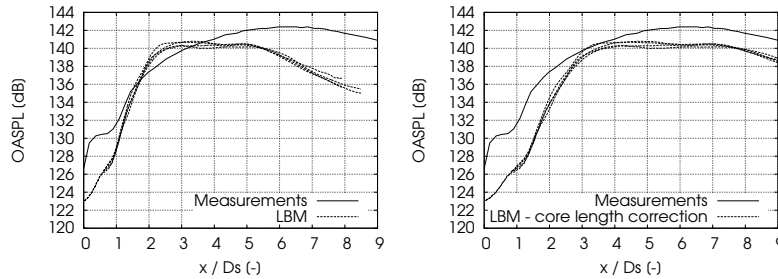


FIGURE 6. OASPL along the near-field microphone array.

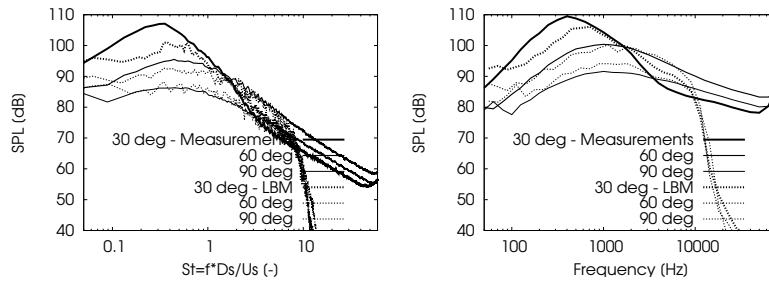


FIGURE 7. Frequency-corrected far-field noise narrow band (left, 50 Hz integration bandwidth) and third-octave band (right) sound pressure level spectra at three radiation angles.

estimated fluctuation levels along the centerline in the range $1 \leq x/D_s \leq 3$ (Figure 4).

5. Acoustic results

This section focuses on the acoustic results. The predicted noise spectra are plotted in Figure 7 and compared to measurements at the same locations. Three radiation angles are considered, as typically done to show the different propagation pattern associated with the noise spectral components. Frequency in the numerical results has been scaled by 70%, based on the assumption that a shorter low-fluctuation core is associated with a higher frequency content (Strouhal similarity). The low-frequency downstream radiation is clearly affected by an underestimation of about 10 dB that may be due in part to a lack of statistical convergence. The grid cutoff takes place at 13 kHz (uncorrected value), which is higher than the nominal expected value of 8 kHz. Interestingly, the crossing frequency between the spectra at 30° and 60° is well captured by the numerical solution.

A qualitative picture of the instantaneous pressure field is shown in Figure 8. The low-frequency wave components associated with the downstream radiation are clearly evident. It is also possible to observe a significant noise generation from the secondary

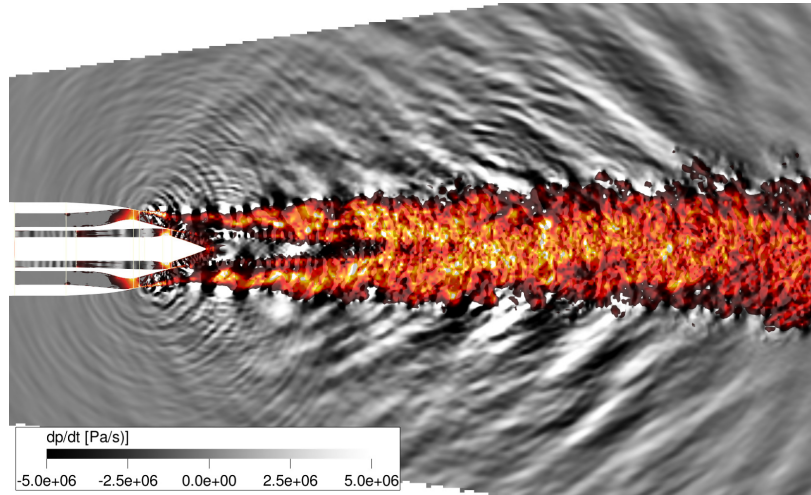


FIGURE 8. Pressure time derivative with superimposed quantity related to Lighthill tensor.

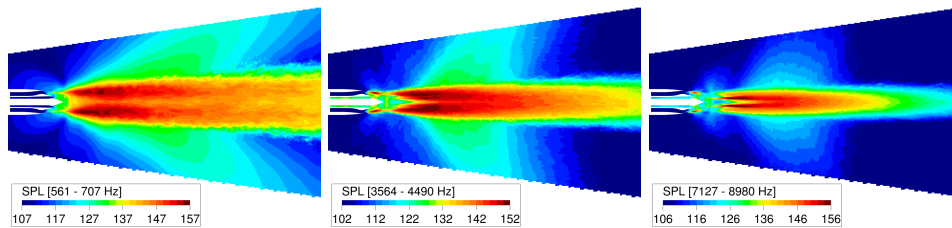


FIGURE 9. Near-field third-octave sound pressure level.

shear layer at about $2 D_s$ downstream of the secondary lip; this is associated with the secondary radiation lobe observed in Figure 6. A specific analysis will be conducted in the future to elucidate the cause of such a modeling artefact.

Finally, contour plots of the near-field sound pressure level are shown in Figure 9. Three third-octave bands have been selected to highlight the varying radiation pattern taking place in the different frequency ranges. As expected, the maximum radiation angle tends to 90° as the frequency is increased. The two higher-frequency bands reveal the presence of strong fluctuations in the initial part of the secondary shear layer, as already observed in Figure 8.

6. Conclusions

A high-speed coaxial flow LBM simulation was carried out using an LBM flow model coupled with a finite-difference solution of the entropy equation. The newly developed formulation is proven to capture the main features of both the flow field and the associated noise radiation, with relatively shorter turnaround times compared to conventional CFD methods. Some deficiencies in the present formulation and/or simulation setup have been pointed out in a premature turbulent breakdown in the shear-layer, and this shortcoming will be the subject of extensive analyses in the future, also involving a mesh resolution study. As long as the formulation is concerned, two main topics need to be addressed: the combined effects of mesh resolution and turbulence model on the shear-layer instabilities, and the effects due to the presence of VR transitions in the plume. As long as the simulation setup is concerned, the effect of the centerbody boundary layer development

on the centerline turbulence levels will be addressed in combination with a random forcing within the nozzles in order to recover the turbulence levels downstream of the centerbody. Moreover, the effect of the uncertainties related to the actual exhaust conditions will be investigated through a parametric study.

Acknowledgments

The authors are grateful to the jet noise group participants of CTR Summer Program 2014, and in particular Peter Jordan, for their valuable comments and review. All CTR members are gratefully acknowledged for their support during the program. The authors also acknowledge the support given by Yanbing Li and other members of Exa Physics Team.

REFERENCES

- ALEXANDER, C. G., CHEN, H., KANDASAMY, S., SHOCK, R. & GOVINDAPPA, S. R. 2001 Simulations of engineering thermal turbulent flows using a lattice Boltzmann based algorithm. *ASME publications* **424**, 115–126.
- ANDERSSON, N., ERIKSSON, L.-E. & DAVIDSON, L. 2005 LES prediction of flow and acoustic field of a coaxial jet. *AIAA Paper 2005-2884*.
- BHATNAGAR, P. L., GROSS, E. P. & KROOK, M. 1954 A model for collision processes in gases. i. small amplitude processes in charged and neutral one-component systems. *Phys. Rev.* **94**, 511–525.
- BOGEY, C., BARRÉ, S., JUVÉ, D. & BAILLY, C. 2009 Simulation of a hot coaxial jet: direct noise prediction and flow-acoustics correlations. *Phys. Fluids* **21**, 1–14.
- BRÈS, G. A., PÉROT, F. & FREED, D. M. 2010 A Ffowcs williams-Hawkings solver for lattice-Boltzmann based computational aeroacoustics. *AIAA Paper 2010-3711*.
- CASALINO, D. 2003 An advanced time approach for acoustic analogy predictions. *J. Sound Vib.* **261**, 583–612.
- CASALINO, D., RIBEIRO, A. F. P. & FARES, E. 2014a Facing rim cavities fluctuation modes. *J. Sound Vib.* **333**, 2812–2830.
- CASALINO, D., RIBEIRO, A. F. P., FARES, E. & NÖLTING, S. 2014b lattice-Boltzmann aeroacoustic analysis of the LAGOON landing gear configuration. *AIAA J.* **52**, 1232–1248.
- CASALINO, D., RIBEIRO, A. F. P., FARES, E., NÖLTING, S., MANN, A., PÉROT, F., LI, Y., LEW, P.-T., SUN, C., GOPALAKRISHNAN, P., ZHANG, R., CHEN, H. & HABIBI, K. 2014c Towards lattice-Boltzmann prediction of turbofan engine noise. *AIAA Paper 2014-3101*.
- CHEN, H., CHEN, S. & MATTHAEUS, W. 1992 Recovery of the Navier-Stokes equations using a lattice-gas Boltzmann method. *Phys. Rev. A* **45** (8), 5339–5342.
- CHEN, H., KANDASAMY, S., ORSZAG, S. A., SUCCI, S. & YAKHOT, V. 2003 Extended Boltzmann kinetic equation for turbulent flows. *Science* **301** (5633), 633–636.
- CHEN, H., TEIXEIRA, C. & MOLVIG, K. 1998 Realization of fluid boundary conditions via discrete Boltzmann dynamics. *Int. J. Mod. Phys. C* **9** (8), 1281–1292.
- CHEN, H. & TEIXEIRA, C. M. 2000 H-theorem and origins of instability in thermal lattice Boltzmann models. *Comput. Phys. Comm.* **129**, 21–31.
- ESCHRICHT, D., YAN, J., MICHEL, U. & THIELE, F. 2008 Prediction of jet noise from a coplanar nozzle. *AIAA Paper 2008-2969*.

- FAYARD, B., RAHIER, G., VUILLOT, F. & KERHERVÉ, F. 2008 Flow field analysis for double stream nozzle: application to jet noise. *AIAA Paper 2008-2983*.
- GUITTON, A., TINNEY, C. E., JORDAN, P. & DELVILLE, J. 2007 Measurements in a co-axial subsonic jet. *AIAA Paper 2007-0015*.
- HABIBI, K., MONGEAU, L., CASALINO, D. & LEW, P.-T. 2014 Aeroacoustic study of internal mixing nozzles with forced lobed mixers using a high-mach subsonic lattice Boltzmann scheme. *AIAA Paper 2014-3313*.
- KHORRAMI, M. R., FARES, E. & CASALINO, D. 2014 Towards full aircraft airframe noise prediction: lattice Boltzmann simulations. *AIAA Paper 2014-2481*.
- KOH, S. R., SCHRÖDER, W. & MEINKE, M. 2009 Noise sources in heated coaxial jets. *19ème Congrès Français de Mécanique*.
- LEW, P.-T., GOPALAKRISHNAN, P., CASALINO, D., SHOCK, R., LE, Y., ZHANG, R., CHEN, H., HABIBI, K. & MONGEAU, L. 2014 An extended lattice Boltzmann methodology for high subsonic jet noise prediction. *AIAA Paper 2014-2755*.
- MARIÉ, S., RICOT, D. & SAGAUT, P. 2009 Comparison between lattice Boltzmann method and Navier-Stokes high order schemes for computational aeroacoustics. *J. Comput. Phys.* **228**, 1056–1070.
- MENDEZ, S., SHOEBY, M., LELE, S. K. & MOIN, P. 2013 On the use of the Ffowcs Williams-Hawkings equation to predict far-field jet noise from large-eddy simulations. *Int. J. Aeroacoust.* **12**, 1–20.
- MIHAESCU, M., GUTMARK, E., SZASZ, R.-Z. & FUCHS, L. 2006 Flow and acoustics of a coaxial nozzle: a sensitivity to the inlet boundary conditions. *AIAA Paper 2006-1387*.
- NIE, X., SHAN, X. & CHEN, H. 2009 A lattice-Boltzmann/finite-difference hybrid simulation of transonic flow. *AIAA Paper 2009-0139*.
- TEIXEIRA, C. M. 1998 Incorporating turbulence models into the lattice-Boltzmann method. *Int. J. Mod. Phys. C* **9**, 1159–1175.
- TINNEY, C. E. & JORDAN, P. 2008 The near pressure field of co-axial subsonic jets. *J. Fluid Mech.* **611**, 175–204.
- TRISTANTO, H., PAGE, G. J. & MCGUIRK, J. J. 2006 Large eddy simulation of hot coaxial jets. *AIAA Paper 2006-2497*.
- SHUR, M. L., SPALART, P. R. & STRELETS, M. K. 2005 Noise prediction for increasingly complex jets. Part I: Methods and tests. *Int. J. Aeroacoust.* **4**, 213–246.
- VISWANATHAN, K. 2004 Aeroacoustics of hot jets. *J. Fluid Mech.* **516**, 39–82.
- VISWANATHAN, K., SHUR, M. L., SPALART, P. R. & STRELETS, M. K. 2006 Computation of the flow and noise of round and beveled nozzles. *AIAA Paper 2006-2445*.
- VUILLEMIN, A., LOHEAC, P., RAHIER, G., VUILLOT, F. & LUPOGLAZOFF, N. 2005 Aeroacoustic numerical method assessment for a double stream nozzle. *AIAA Paper 2005-3043*.
- YAKHOT, V. & ORSZAG, S. A. 1986 Renormalization group analysis of turbulence. i. basic theory. *J. Sci. Comput.* **1**, 3–51.
- YAKHOT, V., ORSZAG, S. A., THANGAM, S., GATSKI, T. B. & SPEZIALE, C. G. 1992 Development of turbulence models for shear flows by a double expansion technique. *Phys. Fluids* **4**, 1510–1520.